Electronic Supplementary Information on:
The INNpinJeR: A new wall-free reactor for studying gas-phase reactions

Wiebke Scholz,*[a], Bernhard Mentler,[a] Lukas Fischer,[a] Torsten Berndt,[b] and Armin Hansel*[a]

S1 ESI - Methods

S1.1 Data and Code availability

The experimental data and plotting scripts associated with this publication as well as input and control files of the openFOAM simulations are available under `https://doi.org/10.5281/zenodo.5713561`.

S1.2 Preparation of SilcoCans containing the VOC

A tetramethyl ethylene (purity $\geq 99\%$, purchased from Sigma-Aldrich) sample was prepared by equilibrating a small pre-evacuated volume of $V_{TME} = 3 \pm 0.05$ mL from the headspace, then isolating the equilibrated volume from the liquid and opening the line to the evacuated SilcoCan (Restek). After that, we filled the SilcoCan with pure nitrogen (Messer Group, purity 5.0) up to $p_{tot} = (4 \pm 0.125)$ bar and left it overnight for equilibration. Thereby we achieved a final concentration of $[\mathrm{TME}] = (6.18 \pm 0.5) \cdot 10^{14}$ molecules cm^{-3} in the SilcoCan.
In the case of cyclohexene, which is less reactive and less volatile, we added liquid cyclohexene (purity 99%, from Sigma-Aldrich), using a standard microlitre syringe ($V_{C_6H_{10}} = 190 \pm 1\ \mu$l), into the SilcoCan inlet onto the closed valve. It was then carried into the SilcoCan with a gas stream by applying $p_{tot} = 4 \pm 0.25$ bar of N_2 to the SilcoCan's inlet and opening the valve. Loss of the substance by evaporation can be excluded and we reached a final concentration of $[C_6H_{10}] = (4.8 \pm 0.4) \cdot 10^{16}$ molecules cm^{-3} within the SilcoCan. Before filling the SilcoCans with the respective reactant, they were cleaned by repetitively evacuating and flushing them with pure nitrogen (purity 5.0, Messer Group) at elevated temperatures of approx. 60°C.

S1.3 Comparable settings of the ammonium chemical ionization mass spectrometer during the cyclohexene experiments at the TROPOS reactor and the INNpinJeR

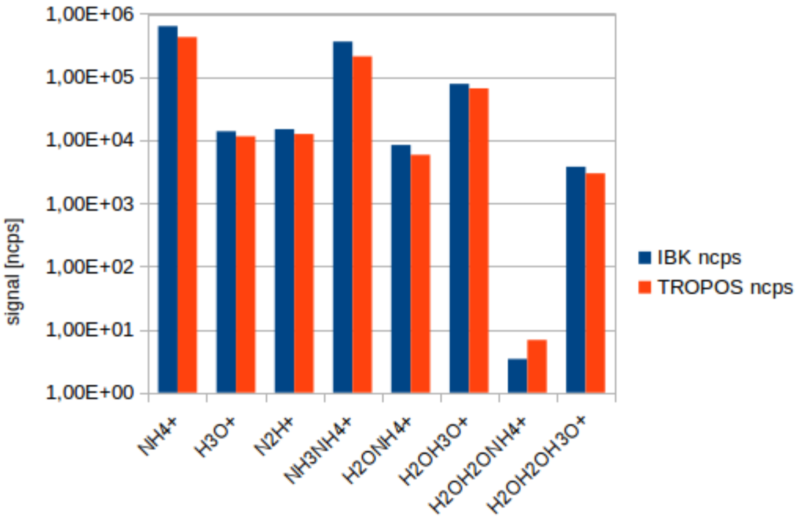

Figure S1 The same instrument settings were used in Innsbruck and at TROPOS as can be seen in the almost identical reagent ion distribution measured. Reagent ion signals are given in normalized count per seconds (ncps).

S1.4 Quantification of the oxidation products

For quantification of the detected products, we first correct each signal of compound *i* for the duty-cycle in the time of flight mass spectrometer, getting

$$\mathrm{dcps(i)} = \mathrm{cps(i)} \cdot \sqrt{\frac{100}{\mathrm{mass(i)}}} \tag{S1}$$

For better comparison of the experiments with a different total ion signal, it is reasonable to normalize the duty-cycle-corrected signals by the total ion signal of all detected primary ions (PI)

$$\mathrm{ncps(i)} = \frac{\mathrm{dcps(i)}}{\mathrm{dcps}(\sum \mathrm{PI})} \tag{S2}$$

where

$$\mathrm{dcps}(\sum \mathrm{PI}) = \sum_{\mathrm{PIs}} \mathrm{cps(PI)} \cdot \sqrt{\frac{100}{\mathrm{mass(PI)}}} \quad \text{, with PI } \in (\mathrm{NH_4}^+, \mathrm{NH_3NH_4}^+, \mathrm{H_2ONH_4}^+). \tag{S3}$$

In table S1 the calibration factors for some directly calibrated compounds are given. In previous publications[1] we assumed that hexanone and heptanone are detected with a sensitivity corresponding to the kinetic limit of the ion molecule reaction rate. Zaytsev *et al.* [2] showed, that this is not the case, but that it is true for decanone (at 3% RH at 20°C, corresponding to a dewpoint temperature $T_{dew} = -27C$), which is detected with a 1.25-times better sensitivity than hexanone. Furthermore they found a somewhat stronger decrease of the hexanone sensitivity with increasing humidity compared to decanone. In our setup, we performed all experiments at even lower humidities at a dewpoint temperature of -50°C. Unfortunately, we were unable to obtain a gas standard including decanone, so that we have to rely on our calibrations with hexanone. We therefore calibrated the oxidation products of cyclohexene with hexanone, corrected by a factor 1.25 to account for Zaytsev *et al.* [2]'s results. This approach comes with an uncertainty due to the different humidities. At lower humidities, we would expect that the factor becomes smaller. By correcting with 1.25 nonetheless, we ensure, that we give lower-limit concentrations of all compounds.

The products of cyclohexene have a similar carbon backbone as hexanone, but have more oxygen-containing functional groups. We therefore expect the uncertainty of the detection efficiency to not exceed 20% as their true detection efficiency is either the kinetic limit, or at least as high as that of hexanone. We correct for the mass-dependent duty-cycle transmission into the TOF, so that this error source can be excluded. Furthermore, by using low energy per collision and therefore no electric field orthogonally to the flow direction, we exclude a mass-dependent transmission of the ions through the IMR due to an orthogonal electric force. The transmission of a non-reactive, volatile ionized compound is also already included

in the calibration factor we obtain for hexanone. By varying the extraction voltages between the IMR and the entry into the TOF lens system, we regularly test whether the observed ion signals are undergoing fragmentation. At high extraction voltages, one can dissociate the ions due to large collision energies (collision-induced dissociation, CID). For cyclohexene peroxy radicals we did observe a decrease of their signals only at significantly higher extraction voltages (see fig. S6) so that we are convinced, that we can exclude their fragmentation under the soft extraction voltage settings we use.
The biggest uncertainty remain losses to surfaces in the inlet or in the IMR. We correct peroxy radicals for inlet line losses which we expect to be efficiently lost upon surface contact but do not correct the accretion products because we do not know how efficiently they are lost to the to the teflon walls of the inlet. Therefore, there is an additional uncertainty of up to +33% for the accretion product concentrations due to inlet line losses. Furthermore, both peroxy radicals as well as some hydroperoxides could be lost to the metal rods in the IMR. We have evaluated this by quantifying how much MVK is artificially formed from ISOPOOH in the instrument and found that approximately 1/3 of ISOPOOH was transformed. MVK was calibrated directly and we calibrated the ISOPOOH relative to MVK by fully converting ISOPOOH to MVK in a metal line. Because of this assumption, this experiment gives us an upper limit for the loss to the metal rods of ca. 33%.

Summarizing, including a typically small statistical mean error $\frac{\sigma}{\sqrt{N}}$, that might play a role for compounds with concentrations close to the limit of detection:

$$\frac{\Delta[\mathrm{RO_2}]}{[\mathrm{RO_2}]} = \frac{\sigma}{\sqrt{N}} \underbrace{+0.3}_{\text{metal rods}} \underbrace{+0.2}_{\text{calibration}} \tag{S4}$$

$$\frac{\Delta[\text{ROOR (LVOC,ELVOC)}]}{[\text{ROOR (LVOC,ELVOC)}]} = \frac{\sigma}{\sqrt{N}} \underbrace{+0.33}_{\text{loss in inlet}} \underbrace{+0.3}_{\text{metal rods}} \tag{S5}$$

Table S1 calibration factors given in duty cycle corrected counts (dcps) per ppb (parts per billion) or norm counts (ncps) per ppb. The norm counts are determined by dividing the dcps/ppb by the summed dcps on all primary ions (dcps($\sum$PI))
The calibration factor of Decanone represents the kinetic limit sensitivity in ammonium mode according to Zaytsev *et al.*[2] and can therefore be used to calibrate all larger and more oxidized molecules.

compound	dcps / ppb	dcps($\sum$PI)	ncps / ppb	rel. to Hexanone	T_{dew}	data obtained from...
Acetone	$2.9 \cdot 10^3$	$4.3 \cdot 10^5$	$0.7 \cdot 10^{-2}$	~0.3	-50°C	calibration during TME experiments
Adipaldehyde			$1.17 \cdot 10^{-2}$	~0.5	-50°C	Hansel *et al.*[1]
Glutaraldehyde			$1.23 \cdot 10^{-2}$	~0.6	-50°C	Hansel *et al.*[1]
Hexanone	$28.1 \cdot 10^3$	$1.25 \cdot 10^6$	$2.2 \cdot 10^{-2}$	-	-50°C	calibration during C_6H_{10}@TROPOS[1]
	$10.2 \cdot 10^3$	$5.2 \cdot 10^5$	$2.0 \cdot 10^{-2}$	-	-50°C	calibration @INNpinJeR
	$54.3 \cdot 10^3$	-	-	-	-27°C	Zaytsev *et al.*[2]
Heptanone	$27.9 \cdot 10^3$	$1.25 \cdot 10^6$	$2.0 \cdot 10^{-2}$	~1	-50°C	calibration during C_6H_{10}@TROPOS[1]
	$10.5 \cdot 10^3$	$5.2 \cdot 10^5$	$2.2 \cdot 10^{-2}$	~1	-50°C	calibration @INNpinJeR
Decanone	$67.8 \cdot 10^3$	-	-	~ 1.25	-27°C	Zaytsev *et al.*[2]

S1.4.1 Uncertainty of the accretion rates due to quantification uncertainties

The k-rates of accretion product formation are determined as the regression slope through points with the x and y values

$$x = \frac{1}{3}[\mathrm{RO_2}] \cdot [\mathrm{R'O_2}] \cdot t_{reac} \tag{S6}$$

$$y = [\mathrm{ROOR'}] \tag{S7}$$

with uncertainties

$$\frac{\Delta x}{x} = 2 \cdot \frac{\Delta \mathrm{RO_2}}{\mathrm{RO_2}} + \frac{\Delta t_{reac}}{t_{reac}} = 2 \cdot (+0.5) \pm 0.11 = +1.11/-0.11 \tag{S8}$$

$$\frac{\Delta y}{y} = +0.83 \tag{S9}$$

these uncertainties lead to a total uncertainty of the accretion rate coefficient of approximately a factor 2:

$$\frac{\Delta k}{k} = -(1 - \frac{1}{1+1.11}) / +0.83 + 0.11 = -0.53 / +0.94 \pm (\frac{\sigma}{N})_{\text{ROOR'}} \tag{S10}$$

Because we only deduce the accretion rates in cases where both peroxy radicals and also their accretion product are well above the limit of detection, statistical errors are small. If any, the statistical error of the ROOR' might play a role in some cases.

S1.5 Mesh for the flow and passive scalar transport simulations with OpenFOAM

To create the domain geometry, we used the open-source tools FreeCAD, version 0.18.4[3] and NetGen[4] to create a mesh that can be transformed into a hex mesh using snappyHexMesh from OpenFOAM. We scaled the cells according to their distance from the closest boundary as well as depending on the boundaries' curvature. This made it possible to create a hex mesh with a very fine resolution close to the jet inlets and in the impingement zone, where the grid cells have edges about three times smaller than the jet diameter, while in the regions down- and upstream, where velocities are significantly smaller, the grid has cells with about 0.5 cm edges. Underrelaxation factors were set to 0.5 for all variables except for the pressure, which was set to 0.3. The link to all initialization files can be found in section S1.1 .

S1.6 2D chemistry simulation

The 2D chemistry simulation runs on the steady state flow field from the OpenFOAM simulation. We use cylindrical coordinates as they describe the situation within the reactor best. Chemical losses or production of the products p are determined with each step δz by

$$\delta[p](z,r)|_{chem} = k\cdot[r_1](z,r)\cdot[r_2](z,r)\cdot\frac{\delta z}{v(z,r)} \tag{S11}$$

with radius r, coordinate in flow direction z, $v(z,r)$ the velocity at each point, k the reaction rate coefficient and $[r_1],[r_2](z,r)$ the concentrations of the reactants at each point. We describe the radial diffusion using Fick's second law. Using that in a flow reactor $\delta t(r,z) = \frac{\delta z(r,z)}{v(r,z)}$, we can rewrite it as changing with z:

$$\frac{dC}{dt} = \frac{D_t}{r}\frac{\partial}{\partial r}(r\cdot\frac{\partial C(r)}{\partial r}) \tag{S12a}$$

$$\Leftrightarrow \frac{dC}{dz} = \frac{D_t}{r}\frac{\partial}{\partial r}(r\cdot\frac{\partial C(r)}{\partial r})\frac{1}{v(z,r)} = \frac{D_t}{r}\cdot(\frac{\partial C(r)}{\partial r}+r\cdot\frac{\partial^2 C(r)}{\partial r^2})\frac{1}{v(z,r)} \tag{S12b}$$

Here C denotes the concentration, r the radius and $v(z,t)$ and $D_t(z,r)$ the steady state velocity field and the effective turbulent diffusivity (see equ. 1) as determined from the OpenFOAM $k-\varepsilon$-RANS flow simulation.

The concentration change of a product p due to diffusion can then be calculated with equ. S12b in numerical form:

$$\delta[p](z,r)|_{diff} \approx \frac{D_t}{r}\cdot(\frac{[p](z,r-\delta r)-[p](z,r+\delta r)}{2\delta r}+r\cdot\frac{[p](z,r-\delta r)+[p](z,r+\delta r)-2[p](z,r)}{\delta r^2})\cdot\frac{\delta z}{v(z,r)} \tag{S13}$$

In each step, we calculate the new concentration of the products by

$$[p](z+\delta z,r) = \underbrace{[p](z,r)}_{\text{advection}}+\underbrace{\delta[p](z,r)|_{diff}}_{\text{diffusion}}+\underbrace{\delta[p](z,r)|_{chem}}_{\text{chemistry}} \tag{S14}$$

In fig S2(a) we show the simulated 2D concentration field of a product of the initial reaction ($k = 1.1\cdot10^{-15}\text{cm}^3\text{s}^{-1}$) and, assuming it is a peroxy radical, its self-reaction accretion product ROOR ($k_{acc} = 1.0\cdot10^{-13}\text{cm}^3\ \text{s}^{-1}$) in fig. S2(b). The reactant concentrations, velocity and diffusivity fields used are taken from a cross-section of the steady state of the 3D $k\varepsilon$ RANS simulation in OpenFOAM. We ensured, that the chemical production of e.g. ROOR from RO_2+ RO_2 is calculated after diffusion of its precursor (the simulated peroxy radical).

In fig. S3 we show radial profiles at different distances from the impingement point. In the simulation we purposefully did not include wall losses, so that the results give us a "worst case" of possible off-centerline production and diffusion back into the centerline. Because ozone is nearly homogeneously distributed in the reactor, the main factors in determining the products' concentration profiles are the VOC distribution and the radially increasing reaction time. The strongly enhanced VOC concentrations close to the centerline compensate the shorter reaction times in the center so that also our product RO_2 from the $VOC + O_3$ reaction is enhanced in the center flow. One can see a light dip in the center directly behind the impingement point that disappears with further distance due to diffusion and weaker gradients of the time coordinate and the VOC. For the ROOR, the accreation product from the RO_2 self reaction, this feature is slightly more pronounced. Because the diffusive flux is directed down the concentration gradient, we can conclude, that inward diffusion of the products takes place in the first few centimeters when their concentrations are still small within a distance < 1cm away from the centerline. Otherwise, diffusion is directed outwards from the center. Inward diffusion of products produced even further outside at larger distances due to the slow flow in the peripheral areas does not reach the center and is therefore

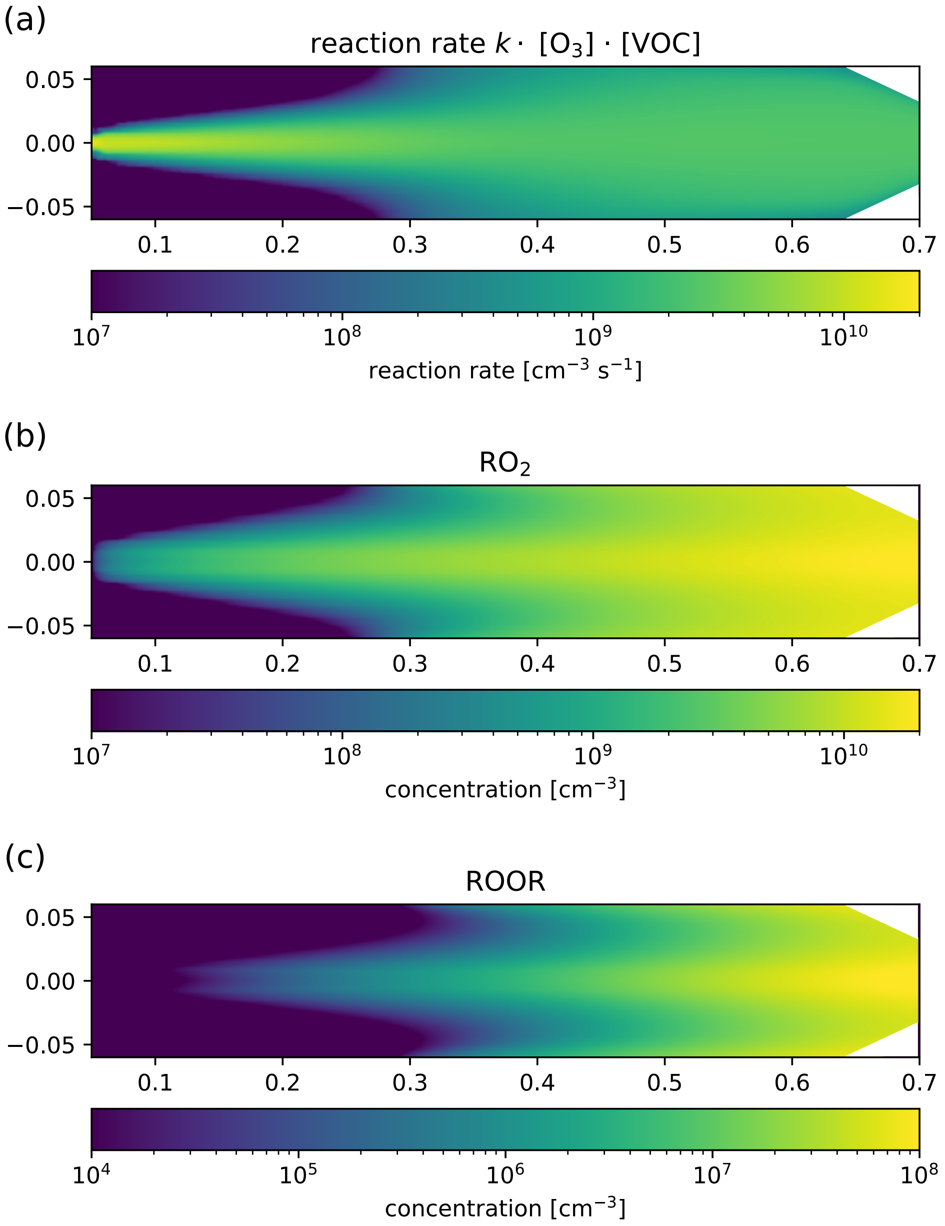

Figure S2 precursor reaction rate (a) and simulated products ((b) an RO_2 (neglecting wall losses) and (c) its accretion product) using a 2D steady state flow field as described in S1.6. Exploiting the symmetry, we only simulated half the area and mirrored it along the centerline for display.

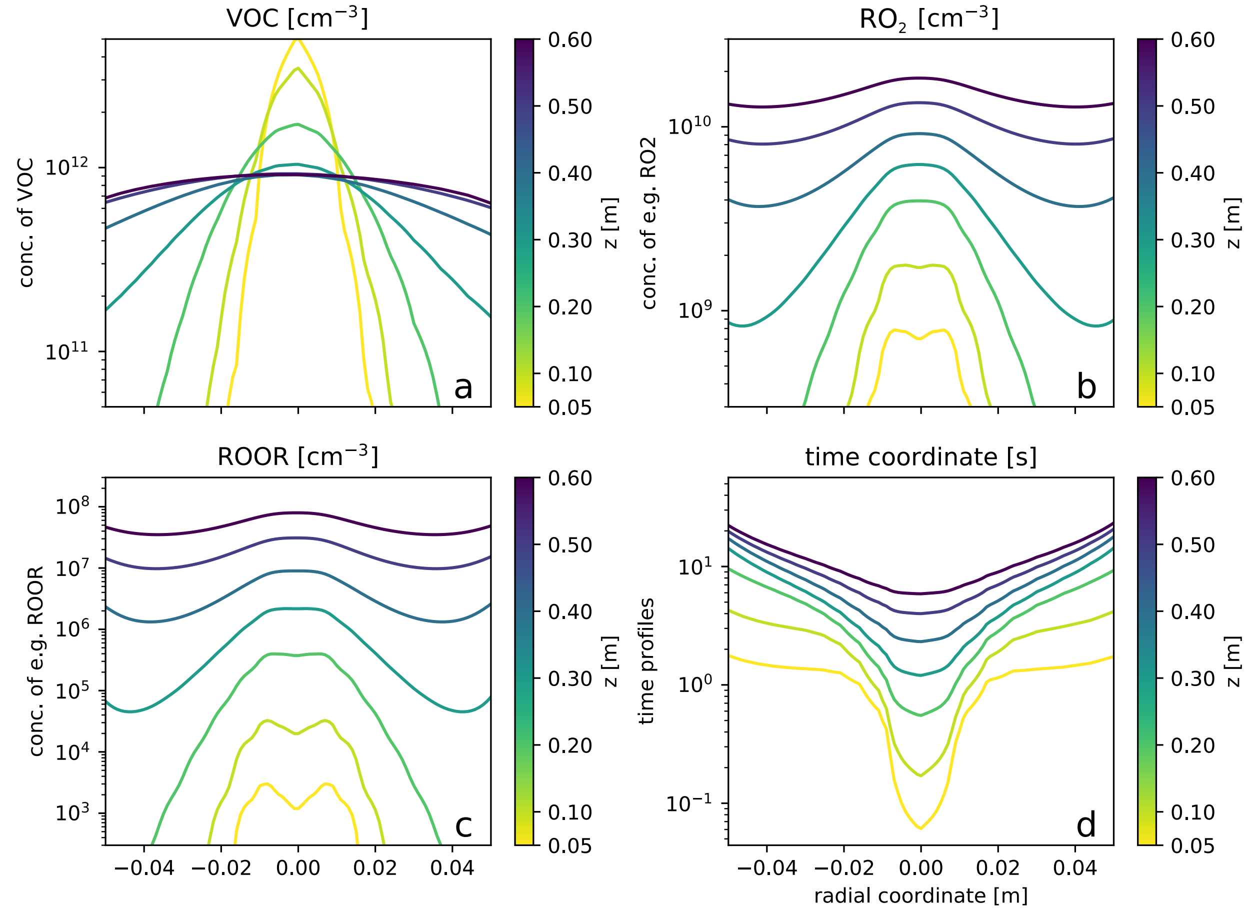

Figure S3 radial profiles through the simulated 2D fields at different z-positions along the centerline of **(a)** the VOC ,**(b)** an example of a peroxy radical RO$_2$ (neglecting wall losses), and **(c)** an ROOR that is formed by self-reaction of the RO$_2$. In **(d)** the time coordinate radial profile is shown. Exploiting the symmetry, we only simulated half the area and mirrored it along the centerline for display.

not relevant for detected products at the centerline.

Finally, we calculated the effective reaction time at each point along the centerline for both simulated example products RO_2 (or Acetone) and the ROOR, using

$$t_{\text{eff,Acetone (or RO}_2)} = \frac{[\text{Acetone}](z, r=0)}{k \cdot [O_3](r=0, z_{\text{end}}) \cdot [VOC](r=0, z_{\text{end}})} \tag{S15}$$

$$t_{\text{eff}} = \left(\frac{3 \cdot [\text{ROOR}](z, r=0)}{k_{acc} \cdot (k \cdot [O_3](r=0, z_{\text{end}}) \cdot [VOC](r=0, z_{\text{end}}))^2}\right)^{1/3} \tag{S16}$$

The results are shown in fig. 4(b).

All other chemistry simulations, where reactants were varied a lot (in the discussion of RO_2 and HO_2 influence), were performed only along the center-line of the reactor as a simple 0D-boxmodel, basically following an air parcel as it travels along the centerline (coordinate z) with the time passed depending on the position. We calculate the product concentration change δp of a product of the first ozonolysis reaction with each time (or space) step by

$$\delta[p(t,z)] = \delta[p(t,z)]_{\text{chem}} - \delta[p(t,z)]_{\text{diffusion}} \tag{S17}$$

with an estimate of the diffusional loss $-\delta[p(t,z)]_{\text{diffusion}}$ determined from the 2D simulation for the example compounds. In each step, the product concentrations are updated:

$$[p(t,z)] = [p(t-\delta t, z-\delta z)] + \delta[p(z,t)] \tag{S18}$$

Using the simulated steady state precursor concentrations from the OpenFOAM simulation is reasonable, as long as the loss of the precursors VOC and O_3, simulated as passive scalars in the OpenFOAM simulation is negligible compared to their concentrations, which is the case for our measurements. Otherwise, their concentrations would need to be adjusted in each timestep due to their chemical losses.
For peroxy radicals formed via OH+VOC, the OH can be calculated similarly, considering its production and loss terms. We do not discuss the OH reactions in great detail throughout the text, because basically all OH formed from cyclohexene ozonolysis is reacting with cyclohexene again to form just another peroxy radical with sumformula $HO{-}C_6H_{10}O_2$, that then undergoes reactions with RO_2 and HO_2. We already showed in Hansel *et al.* [1] that we detect the peroxy radical with a concentration close to the simulated total OH produced. For the TME + O_3 system, reaction conditions are similar.

S2 ESI - Results

S2.1 The nature of $C_5H_9O_3$

The ozonolysis of cyclohexene reveals a compound detected at the exact mass of $C_5H_9O_3 \cdot NH_4^+$, which could be a not yet recognized peroxy radical. We detect accretion products ROOR', which indicate the existence of $C_5H_9O_3$ peroxy radicals. Fig. S4 shows the linear correlation of the $C_{11}H_{20}O_4$ ROOR' accretion product versus the product of its peroxy radical building blocks $C_5H_9O_3$ and $C_6H_{11}O_3$. This is an example obtained from the TROPOS reactor with an effective reaction time of 7.9 s.

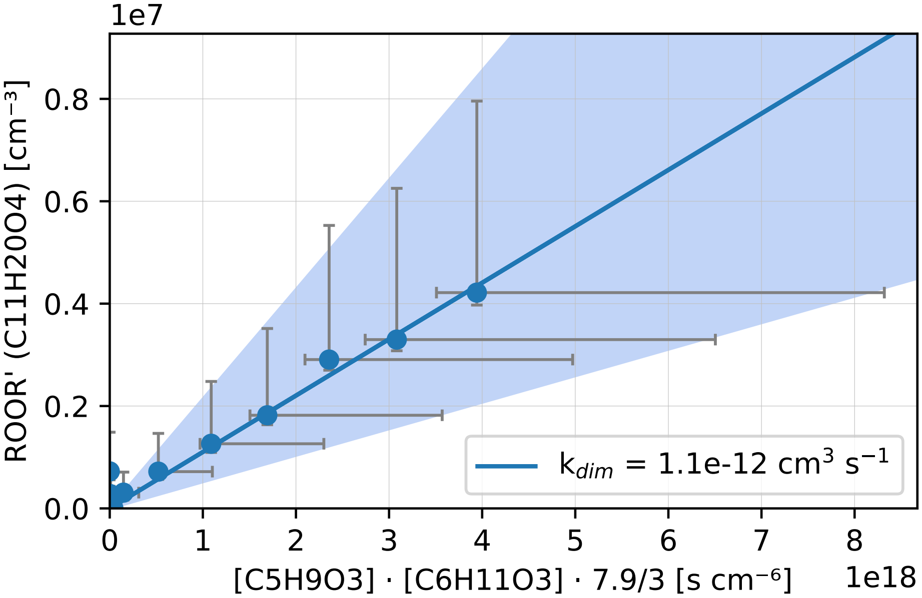

Figure S4 The formation of an accretion product from $C_5H_9O_3$ and $C_6H_{11}O_3$ peroxy radicals. The accretion product is plotted against the product of outflow concentrations of the two peroxy radicals times the reaction time of 7.9 seconds in the TROPOS reactor and divided by 3. Then, according to equ. S37 , the slope of the fit corresponds to the accretion rate coefficient k_{dim}. The shaded area depicts the uncertainty of k_{dim} due to the possible systematic errors of the peroxy radicals and their accretion product (see sec. S1.4)

We added NO $(0.15-1.9)\cdot 10^{10}$ cm^{-3} to the INNpinJeR main flow right before entering the reactor during a cyclohexene ozonolysis experiment (at T = 293 ± 2 K, ozone $1.7\cdot 10^{12}$ cm^{-3}, cyclohexene $6\cdot 10^{11}$ cm^{-3}). It is well known that peroxy radicals react with NO forming organonitrates (equ. S19a) and $RO+NO_2$ (equ. S19b) with typical reaction rate coefficients of a few 10^{-11} cm^3 s^{-1}.

$$RO_2 + NO \xrightarrow{y_{RONO_2}} RONO_2 \tag{S19a}$$

$$\xrightarrow{y_{RO+NO_2}} RO + NO_2 \tag{S19b}$$

Fig. S5 shows recorded signals of selected peroxy radicals and corresponding organonitrates detected as ammonium ion clusters, respectively. We can clearly see a decrease of peroxy radicals and an increase of corresponding organonitrates. Further addition of NO to the reactor would change the reaction conditions. Therefore we cannot convert RO_2 radicals into $RONO_2$ completely. The observed decrease of the $C_5H_9O_3$ signal when NO is added is a clear indication that the $C_5H_9O_3$ signal at least partly consists of a peroxy radical. By performing ramps of the collision-induced dissociation voltages (see fig. S6), we did not observe a decay of any of the larger peroxy radicals, that might have fragmented on the exact mass of $C_5H_9O_3$, before the ammonium-water clusters decay. This suggests, that the peroxy radicals themselves as well as their ammonium clusters are stable enough to survive the ionization and transfer into the TOF.

In an experiment, where we added propane as OH scavenger to the TROPOS reactor, presented previously by Hansel *et al.* [1], the signal of $C_5H_9O_3$ decreased by roughly 20%, suggesting that 80% of the signal is produced by the cyclohexene + ozone reaction (as is e.g. $C_5H_9O_5$). At present we cannot suggest a conclusive pathway leading to $C_5H_9O_3$ peroxy radicals.

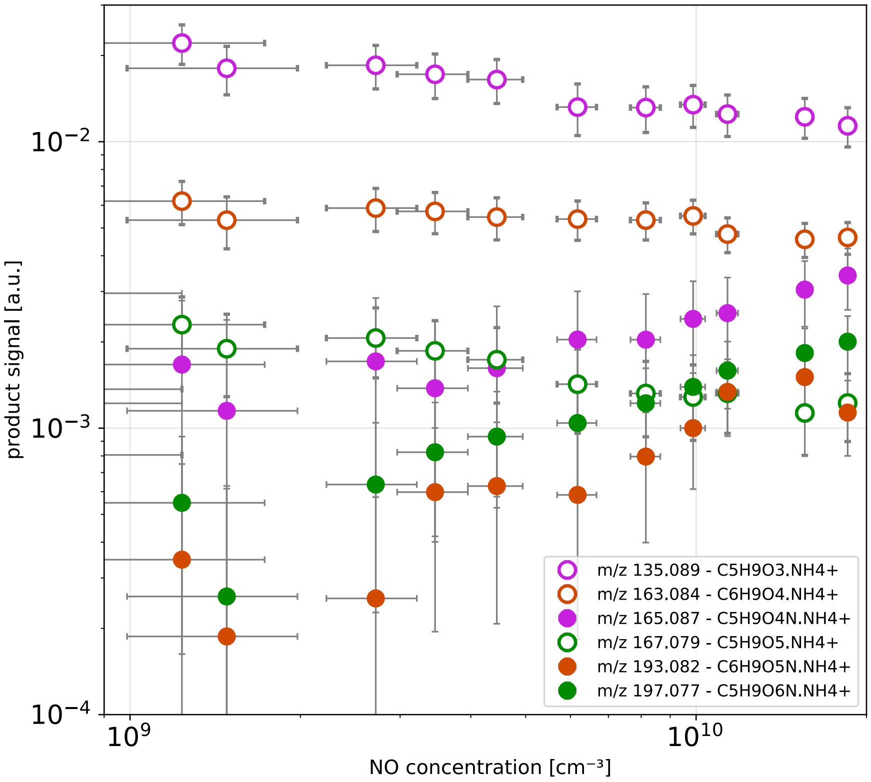

Figure S5 Peroxy radical concentrations (open symbols) and corresponding organonitrates (solid symbols) as a function of NO addition to the reactor. The NO concentration was measured with a NOx monitor (Thermo Environmental Instruments 42 iQ). Error bars show the standard deviation of the data for each stage.

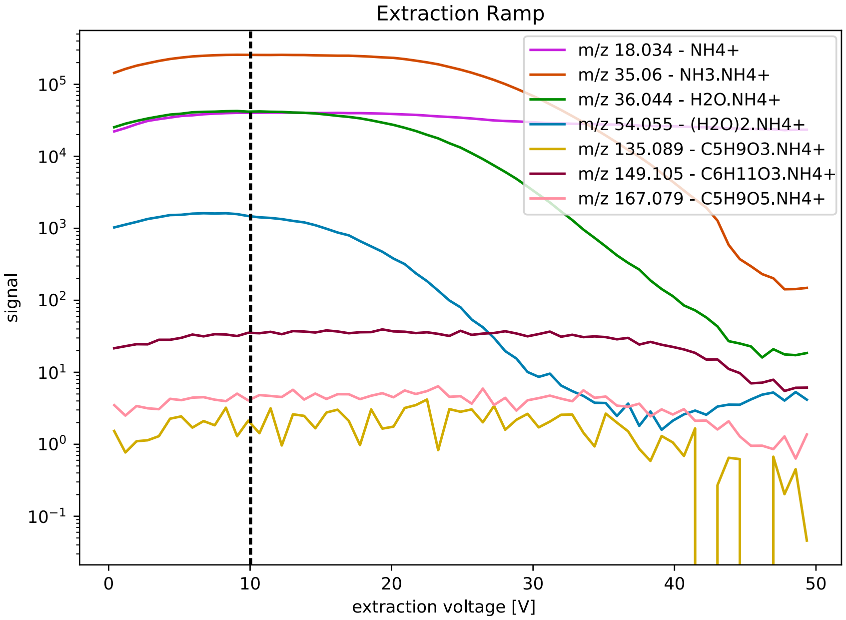

Figure S6 shows an "Extraction Ramp" for the cyclohexene oxidation products. More precisely the ion signals (a.u.) are shown as a function of the extraction voltage. With increasing voltage, the ammonium-water clusters fragment and their signals decay, starting with the weakest bound cluster, containing two water clusters (blue). We observe a decay of the peroxy radical signals not before even the ammonia-ammonium cluster (dark orange) fragments, which shows that the stability of the ammonium RO_2 clusters as well as the RO_2 themselves, is high enough so that fragmentation can be excluded under our experimental settings of typically 10V (shown as vertical line).

S2.2 Additional explanation of the effect of HO_2 and RO_2 radical concentrations on measured accretion rates (fig. 8 in the main text)

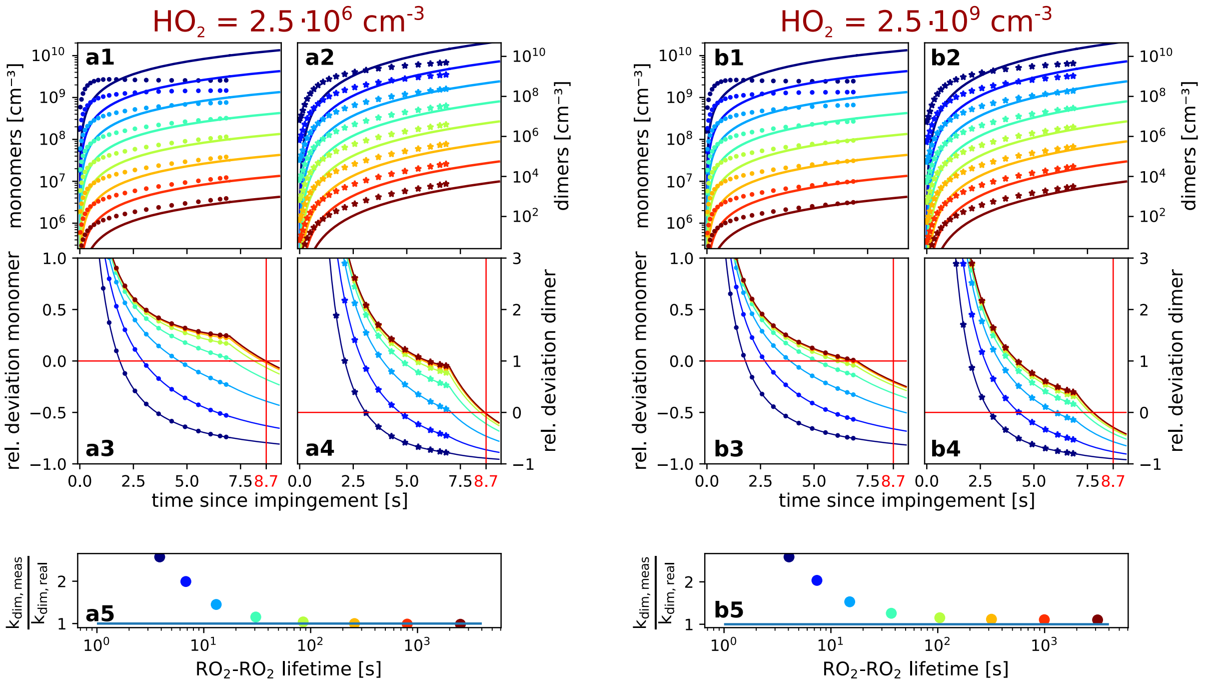

Figure S7 Effect of reactant inhomogeneity on radicals and their corresponding accretion products for different RO_2 lifetimes with respect to the reaction with other peroxy radicals (corresponding to the different colors) and comparison with ideal behaviour for low (a) and high (b) HO_2 concentrations. In plots a1, a2, b1 and b2, the lines depict the ideal behaviour of the products, while the dots and stars show the simulated concentrations.

Figure S7 shows the differences between simulated behaviour of the peroxy-radicals (monomers) and accretion products (dimers) compared to their "ideal" linear and quadratic behaviour for two different HO_2 concentrations and different $RO_2{-}RO_2$ lifetimes. It is added for a more detailed analysis of how the data in fig.8 emerge. Figures S7 a5) and b5) present the HO_2-specific results as depicted as well in fig.8. Figures S7 a1) and b1) show the simulated (dots) and ideal (lines) behaviour of summed peroxy radicals with different yields (and thereby different $RO_2 + RO_2$ lifetimes due to reactions with each other). Figures S7 a2) and b2) show the corresponding sum of accretion products. In figures S7 a3) and b3) for the peroxy radicals (in figs. S7 a4) and b4) for accretion products) the respective deviation of the simulated behaviour from the ideal curve is shown. The kinks in the lines occur, because the final data point is copied in time to see, when it would equal the ideal behaviour (and the deviation equals zero). While for low HO_2 and long RO_2 lifetimes, the crossing occurs at 8.7s for both peroxy radicals and accretion products, this is no longer the case for short $RO_2 + RO_2$ lifetimes and high HO_2 concentrations. Finally in figs. S7 a5) and b5) the error on accretion kinetics that one would make assuming ideal behaviour of all products is shown. While HO_2 in this concentration range only has a minor effect, too high RO_2 concentrations can significantly enhance the apparent accretion rates.

In panels a1 and b1 of fig. S7 the RO_2 concentrations are shown dotted as simulated and as lines assuming a linear increase. Figs. S7 a2) and b2) show the same for accretion products ROOR' with the difference that the ideal behaviour is now cubic in time, according to equ. S37.

It is apparent, that the concentrations of both, the modeled primary and secondary products are strongly enhanced compared to an idealized increase in the first two seconds due to the high reactant concentrations close to the impingement point. During the further reaction time the deviation from the assumed ideal behaviour decreases as the reaction slows down due to lower reactant concentrations and enhanced losses by bimolecular reactions, as radical concentrations increase. The losses play a role only for the runs with very high RO_2 concentrations. The major effect in runs with long radical lifetimes is foremost the non-constant precursor concentrations. When the lifetime of the radicals becomes smaller than the reaction time, the RO_2-concentration levels out towards a steady state between production and losses. For low HO_2 concentrations and long $RO_2{-}RO_2$ lifetimes, we find, that the deviation (shown in figs. S7 a3, b3, a4, b4) would be zero at the effective reaction time of 8.7s in the reactor (the reaction time in further inlet lines was excluded in the simulation). That shows, that the enhanced reactant concentration in the first seconds is not influencing the results, when the effective reaction time is used for analysis. For shorter RO_2-RO_2 lifetimes we find an ever-growing deviation from the idealized behavior, because of the formation of an equilibrium state. Therefore high reactant concentrations can induce errors, when deriving kinetic information from the experimental data. In figures S7 a5) and b5), we show the error for deriving accretion rates from the data. As long as lifetimes are significantly longer than the reaction time, the induced systematic error is negligible, but increases exponentially towards short RO_2-RO_2 lifetimes compared to the reaction time. Since short lifetimes affect the RO_2 concentrations at the outflow stronger than the product concentrations, accretion rates deduced from such experiments would be systematically too high. In fig. S7 b5) the concentration of HO_2 is close to the highest HO_2 concentration possible in our reactor (see sec. S2.3). This enhanced HO_2 background increases the loss rates of the RO_2-radicals, thereby reducing their lifetimes. Nonetheless, assuming a typical reaction rate constant of $2.2\cdot10^{-11}\text{cm}^3\text{s}^{-1}$ between RO_2 and HO_2, the effect is still minor for a concentration of $2.5\cdot10^{9}\text{cm}^{-3}$ and affects the deduced rate constants only by a few percent.

S2.2.1 Analytical investigation of the effect of high RO_2 and HO_2 concentrations in our reactor for two special cases

Fig. 8 and fig. S7 show the effect of enhanced RO_2 and HO_2 concentrations. It is based upon numerical calculations along the centerline, as described in sec. S1.6. To ensure that the results of the numerical simulation, shown in fig. 8 make sense, we are now looking at two special cases which we solve analytically. These are:

- high but constant HO_2 concentrations and low RO_2 concentrations
- high RO_2 concentrations and negligible HO_2 concentrations

We choose these two cases to be able to solve them analytically and to show the respective separated effects on inferred accretion rate coefficients.
To simplify our system for this analytical approach as much as possible, we ignore any further reactions leading to loss or production of HO_2 and RO_2 and describe our dark reaction system (without NO) approximately as

$$\frac{\mathrm{d}}{\mathrm{dt}}[\mathrm{RO_2}] = k_3\cdot y_{\mathrm{RO_2}}\cdot[\mathrm{O_3}][\mathrm{VOC}] - k_4\cdot[\mathrm{HO_2}][\mathrm{RO_2}] - k_5\cdot([\mathrm{RO_2}])^2 \tag{S20a}$$

$$\frac{\mathrm{d}}{\mathrm{dt}}[\mathrm{HO_2}] = -k_4\cdot[\mathrm{HO_2}][\mathrm{RO_2}] \tag{S20b}$$

$$\frac{\mathrm{d}}{\mathrm{dt}}[\mathrm{ROOR}] = y_{\mathrm{ROOR}}\cdot k_5\cdot([\mathrm{RO_2}])^2 \tag{S20c}$$

Equ. S20c does not influence the other equations.

To solve it analytically, we simplify our system, assuming that during the time of interest

$$\int_0^{\mathrm{t}} \frac{\mathrm{d}}{\mathrm{d}\tau}[\mathrm{HO_2}]\mathrm{d}\tau \ll [\mathrm{HO_2}]_0 \tag{S21}$$

and that precursor concentrations stay constant as well. Then equ. S20a (using shorter symbols) is of the form

$$\frac{\mathrm{d}}{\mathrm{dt}}x = a - b\cdot y\cdot x - c\cdot x^2 \tag{S22}$$

with a,b,c being constants and x and y refer to the RO_2- and HO_2-concentration (also assumed constant), respectively. Let's investigate two separate cases. First, let the RO_2-concentration be small, but assume a non-negligible HO_2-concentration, so that $c\cdot x^2 \ll b\cdot y\cdot x \sim a$, leading to the even simpler form

$$\frac{\mathrm{d}}{\mathrm{dt}}x = a - b\cdot y\cdot x \tag{S23}$$

Separation of the variables and integration leads to x(t):

$$\int_0^x \frac{1}{a-b\cdot y\cdot\chi}d\chi = \int_0^t dt$$

$$\Leftrightarrow \frac{-1}{b\cdot y}\cdot\ln\left(\frac{a-b\cdot y\cdot x}{a-b\cdot y\cdot 0}\right) = t$$

$$\Leftrightarrow x(t) = \frac{a}{b\cdot y}(1-\exp(-b\cdot y\cdot t)) \tag{S24}$$

Which is a function that increases evermore slowly from zero for $t = 0$ up to the equilibrium value $\frac{a}{b\cdot y}$ for $t \to \infty$. Taylor-expansion for the specific cases $(b \cdot y) \to 0$ or $t \to 0$, so that $(b \cdot y \cdot x \ll a\ )$ gives

$$x(t,(b\cdot y)\to 0) \approx a\cdot t \tag{S25}$$

Starting again from equ. S22, but assuming this time a negligible HO_2-concentration and RO_2-concentrations high enough, so that

$$\frac{\mathrm{d}}{\mathrm{dt}}x = a - c\cdot x^2 \tag{S26}$$

Again, separation of the variables and integration by substituting $\sqrt{\frac{-c}{a}}\cdot\chi = \upsilon$ leads to:

$$\begin{aligned}
&\int_0^x \frac{1}{a - c\cdot\chi^2}d\chi = \int_0^t dt\\
&\Leftrightarrow \int_0^u \frac{1}{(a\upsilon^2 + a)}\sqrt{\frac{a}{-c}}\,\mathrm{d}\upsilon = \frac{1}{\sqrt{a\cdot(-c)}}\int_0^u \frac{1}{\upsilon^2+1}\,\mathrm{d}\upsilon = t\\
&\Leftrightarrow \frac{\arctan(u)}{\sqrt{a\cdot(-c)}} = \frac{\arctan(\sqrt{\frac{-c}{a}}\cdot x)}{\sqrt{a\cdot(-c)}} = t\\
&\text{with } c,a,t,x > 0\ :\ \frac{i\cdot\tanh^{-1}(\sqrt{\frac{c}{a}}\cdot x)}{i\cdot\sqrt{a\cdot c}} = t\\
&\Leftrightarrow x(t) = \tanh(\sqrt{a\cdot c}\cdot t)\cdot\sqrt{\frac{a}{c}}
\end{aligned} \tag{S27}$$

Also this function increases evermore slowly from zero for $t = 0$ up to an equilibrium value $\sqrt{\frac{a}{c}}$ for $t \to \infty$. Taylor-expansion for the specific case, that $t \to 0$ (where $c\cdot x^2 \ll a$) gives

$$x(t\to 0) \approx a\cdot t \tag{S28}$$

For both non-negligible $RO_2 + RO_2$ as well as for $RO_2 + HO_2$ reactions, the RO_2-concentration will at some point deviate from a linear increase and run towards a steady-state.

When analyzing accretion rate coefficients by inferring it from detected accretion product to its precursor peroxy radical ratios, this should be thought of. In previous publications, we analyzed small enough times and reactant concentrations, so that $[RO_2](t) \approx a\cdot t$, so that we could calculate the accretion rate constant from detected outflow accretion product and peroxy radical concentrations: Let's call $y_{ROOR}\cdot k_5! = k_{dim}$ from equ. S20c and integrating equ. S20c from 0 to time t under the assumption, that $[RO_2](t) \approx a\cdot t$, we find that

$$[\mathrm{ROOR}](t) \approx \frac{k_{dim}[RO_2]^2 t}{3} \quad\Leftrightarrow\quad k_{dim} \approx \frac{3[\mathrm{ROOR(t)}]}{[RO_2(t)]^2\cdot t} \tag{S29}$$

In case of too high HO_2 (or RO_2) concentrations, when the first order Taylor approximation is not valid anymore, one would introduce an error by using the approximation in equ. S29. For simplicity, let's write equ. S20c again in a more symbolic way:

$$\begin{aligned}
&\frac{\mathrm{d}}{\mathrm{dt}}z = \gamma\cdot x(t)^2\\
&\Leftrightarrow z(t) = \gamma\int_0^t (x(\tau))^2 d\tau
\end{aligned} \tag{S30}$$

compared to the approximation

$$z(t) \approx \frac{\gamma}{3}x(t)^2\cdot t \tag{S31}$$

In the first case with high HO_2 concentration, but low RO_2 concentrations, x(t) is described by equ. S24, so that

$$
\begin{aligned}
z(t) &= \gamma \frac{a^2}{b^2 \cdot y^2} \int_0^t (1-\exp(-b \cdot y \cdot \tau))^2 d\tau \quad \text{,substituting} \quad -b \cdot y \cdot \tau = \upsilon \\
&= \gamma \frac{a^2}{b^2 \cdot y^2} \cdot (\frac{-1}{b \cdot y}) \int_0^u (\exp(\upsilon)-1)^2 d\upsilon \\
&= \gamma \frac{a^2}{b^2 \cdot y^2} \cdot (\frac{-1}{b \cdot y}) \cdot (\int_0^u \exp(2\upsilon) d\upsilon - 2\int_0^u \exp(\upsilon) d\upsilon + \int_0^u 1 d\upsilon) \\
&= \gamma \frac{a^2}{b^2 \cdot y^2} \cdot (\frac{-1}{b \cdot y}) \cdot (\frac{\exp(2u)}{2} - 2\exp(u) + u - \frac{1}{2} + 2) \\
&= \gamma \frac{a^2}{b^2 \cdot y^2} \cdot (\frac{-1}{b \cdot y}) \cdot (\frac{1}{2}\exp(-2b \cdot y \cdot t) - 2\exp(-b \cdot y \cdot t) - b \cdot y \cdot t + 1.5) \qquad \text{(S32)}
\end{aligned}
$$

In the second case with high RO_2 concentrations, but negligible γ, $x(t)$ is described by S27, so that

$$
\begin{aligned}
z(t) &= \gamma \cdot \frac{a}{c} \cdot \int_0^t \tanh^2(\sqrt{a \cdot c} \cdot \tau) \cdot d\tau \\
&= \gamma \cdot \frac{a}{c} \cdot (t - \frac{\tanh(\sqrt{a \cdot c} \cdot t)}{\sqrt{a \cdot c}}) \qquad \text{(S33)}
\end{aligned}
$$

In fig. S8 the analytical solutions for the different cases for peroxy radicals are plotted. In fig. S9 the analytical solutions are plotted as solid lines, together with estimated accretion product concentrations from calculated peroxy radicals $x(t)$ according to equ. S31. To create these plots, values as summarized in table S2 have been used for the different constants. We find that the approximated formula (equ. S31) underestimates the accretion product concentrations for non-negligible losses by reactions with RO_2 and HO_2 - meaning that an accretion rate coefficient inferred from experimental results would accordingly be overestimated in those cases. The higher RO_2 and/or HO_2 concentrations are, the larger this overestimation becomes. In reality (and in the numerical simulation) both effects are intertwined.

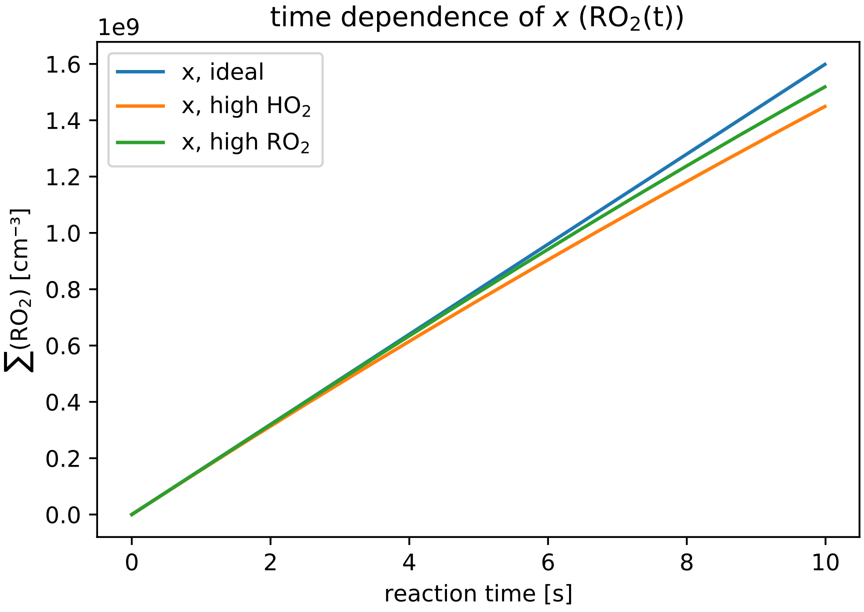

Figure S8 time dependent analytical solutions for peroxy radical concentrations in case of no significant losses (blue), only losses due to reactions with HO_2 and neglecting RO_2 (orange, equ. S24) and due to reactions with RO_2 while neglecting HO_2 (green, equ. S27)

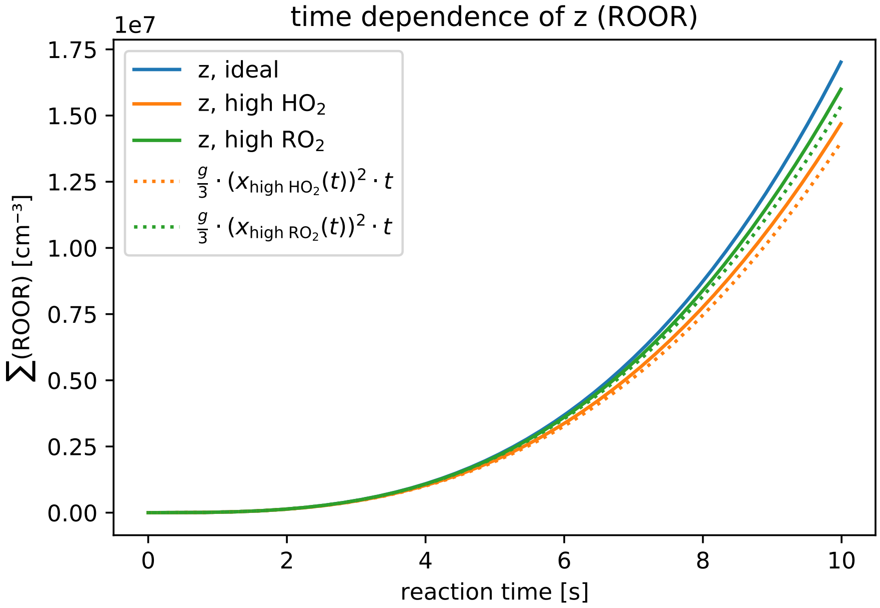

Figure S9 time dependent analytical solutions for summed accretion product concentrations (solid lines) in case of no significant losses of peroxy radicals (blue, equ. S31 with $x(t) = a \cdot t$), only losses of peroxy radicals due to reactions with HO_2, neglecting RO_2 (orange, equ. S32) and due to reactions with RO_2, neglecting HO_2 (green, equ. S33). As dotted lines is shown, how large accretion products would be as estimated from peroxy radical concentrations in the different cases, that is equ. S31) with $x(t)$ from equ. S24 (orange) and with $x(t)$ from equ. S27 (green).

Table S2 summarized constants used for figures S8 and S9

variable	refers to... in reaction system (S3a,b,c)	meaning	value	unit
a	$k_3 \cdot y_{RO_2} \cdot [O_3]\ [C_6H_{10}]$	RO_2 production rate	$1.6 \cdot 10^8$	s^{-1}
c	k_5	reaction rate coefficient of $RO_2 + RO_2$	$1 \cdot 10^{-11}$	$cm^3\ s^{-1}$
γ	$y_{ROOR} \cdot k_5$	ROOR production rate coefficient	$2 \cdot 10^{-12}$	$cm^3\ s^{-1}$
b	k_4	reaction rate coefficient of $RO_2 + HO_2$	$2 \cdot 10^{-11}$	$cm^3\ s^{-1}$
y	$[HO_2]$	HO_2 concentration	$1.0 \cdot 10^9$	cm^{-3}

S2.3 Estimation of the highest possible HO_2 concentration during the cyclohexene experiments

In the main part we assumed an HO_2 concentration of $[HO_2] \leq 2 \cdot 10^9$ cm^{-3}. This number is based on the ratio of the RO_2 radical detected as $(HO{-}C_6H_{10}O_2)NH_4^+$ and the corresponding peroxide ROOH detected as $(C_6H_{12}O_3)NH_4^+$ cluster ions. This ratio is approximately constant as can be seen in figure S10. A similar value was found from the calculation of HO_2 formation in the ozone generator (see sec. S2.3.1), when assuming a water concentration of $[H_2O] = 10^{15}$cm^{-3}. This water concentration corresponds to a dewpoint of approximately −50°C, which actually is the case for the air at the exit of the pressure swing adsorption stage. We would expect that the air is dried even further in the molecular sieves, which follow.

We are focusing for this discussion on $HO{-}C_6H_{10}O_2$ and the corresponding hydroperoxide (ROOH) with formula $C_6H_{12}O_3$. A drawback of mass spectrometry is, that while the chemical formula is clearly determined, we do not know the structure of the molecule. We assume the whole signal with formula $C_6H_{12}O_3$ to be the hydroperoxide of $HO{-}C_6H_{10}O_2$, because so far no other pathway then reaction 4 is known. Fig. S10 shows $HO{-}C_6H_{10}O_2$ and its corresponding hydroperoxide together with the accretion product of the $HO{-}C_6H_{10}O_2$ self-reaction. We observe, that apart from very high C_6H_{10} reaction rates, when additional losses of the peroxy radical become non-negligible, both the hydroperoxide and the peroxy radical are increasing approximately linearly. The ratio of the signals ROOH / RO_2 is approximately constant as a function of cyclohexene (fig. S10 a) as well as a function of ozone (fig. S10 b). That means that HO_2 would be produced independently of reacted cyclohexene and we can estimate the HO_2 concentration required to produce the ROOH by integrating equ. 4:

$$[\mathrm{ROOH}](\tau) = k_{\mathrm{HO_2}}[\mathrm{HO_2}] \int_0^{\tau} [\mathrm{RO_2}]dt \tag{S34}$$

Approximating $[RO_2](t) \propto t$ in equ. S34 yields

$$[\mathrm{ROOH}](\tau) \approx \frac{1}{2} k_{\mathrm{HO_2}}[\mathrm{HO_2}][\mathrm{RO_2}](\tau) \cdot \tau \tag{S35}$$

and the ratio of RO_2 and ROOH can give us an idea about the HO_2 concentration. Solving equ. S35 for HO_2 and using $\frac{[\mathrm{ROOH}](\tau)}{[\mathrm{RO_2}](\tau)} \approx 0.2$, $k_4(T \approx 300K) \approx 2.2 \cdot 10^{-11}\mathrm{cm^3 s^{-1}}$ and $\tau \approx 9.4$ s, we would get a required HO_2 concentration of $[HO_2] \approx 2 \cdot 10^9 \mathrm{cm^{-3}}$ to explain the observed $C_6H_{12}O_3$ concentrations. For the signals with formulas $C_5H_{10}O_{3,5,7}$ and $C_6H_{10}O_{4,6,8}$ (presumably the hydroperoxides of the radicals $C_5H_9O_{3,5,7}$ and $C_6H_9O_{4,6,8}$), other formation pathways (e.g. via equ. 5c) might exist. Nonetheless, we observed similar ratios and qualitative behaviors for these RO_2 and ROOH pairs as for the shown signals of $(HO{-}C_6H_{10}O_2)NH_4^+$ and $(C_6H_{12}O_3)NH_4^+$.

As will be discussed in section S2.3.1, the constant ROOH/RO_2 ratio as a function of increasing ozone cannot conclusively be explained. If HO_2 production by water photolysis in the ozone generator (see section S2.3.1) would be important, a hydroperoxide should increase steeper than linearly with increasing ozone, as HO_2 would increase as well.

S2.3.1 Estimated HO_2 production in the ozone generator

The UVP ozone generator uses 185 nm UV light to produce 3.0 ppm ozone in a lighted length of 9 inches (22.86 cm) at a flow rate of 1.0 slpm air. The light intensity at 185 nm is about 20 mW/cm^2 and 4 mW/cm^2 at 254 nm, respectively. The photolysis rate $J_{M,\lambda}$ of a molecule M at a wavelength λ is calculated by multiplying the absorption cross-section $\sigma_{M,\lambda}$ with the quantum yield (here: one for all molecules) and the photon flux at the respective wavelength, which is the ratio of the light intensity I_λ and the energy per photon, according to equ. S36:

$$J_{M,\lambda} = \sigma_{M,\lambda} \cdot I_\lambda \cdot \frac{\lambda}{hc} \tag{S36}$$

Table S3 summarizes all relevant data for simulating the photolysis in the ozone generator. and implemented the photolysis reactions and a model for the cyclohexene ozonolysis with the reactor-specific features.

In fig. S11 we show the simulation result of the hydroperoxy radical concentration over the reaction time. The illuminated stage 1 (O_3 generator) produces nearly 10^{11} molecules cm^{-3} HO_2 by water photolysis assuming a H_2O concentration of 10^{15} cm^{-3} and via OH formation. HO_2 reacts further with CO, that we assumed to be about 10^{13} molecules cm^{-3}, with O_3 and with itself. In stage 2, the products from stage 1 react further in darkness before they get diluted with the main flow. Stage 2 was very short (0.4s) in our setup. The HO_2 concentration decreases in this stage mainly due to self-reactions that lead to H_2O_2. To reduce HO_2 in the reactor, one could therefore try to increase the time in stage 2, as H_2O_2 is less reactive and therefore not as important in the further reaction. The dilution factor is 35 when mixed with the main flow, which happens immediately in the simulation. That means, that after dilution, the HO_2 self-reaction is decreased by ca. a factor 1000. Stage 3 corresponds to the time in which the laminar flow profile develops in the first part of the INNpinJeR.

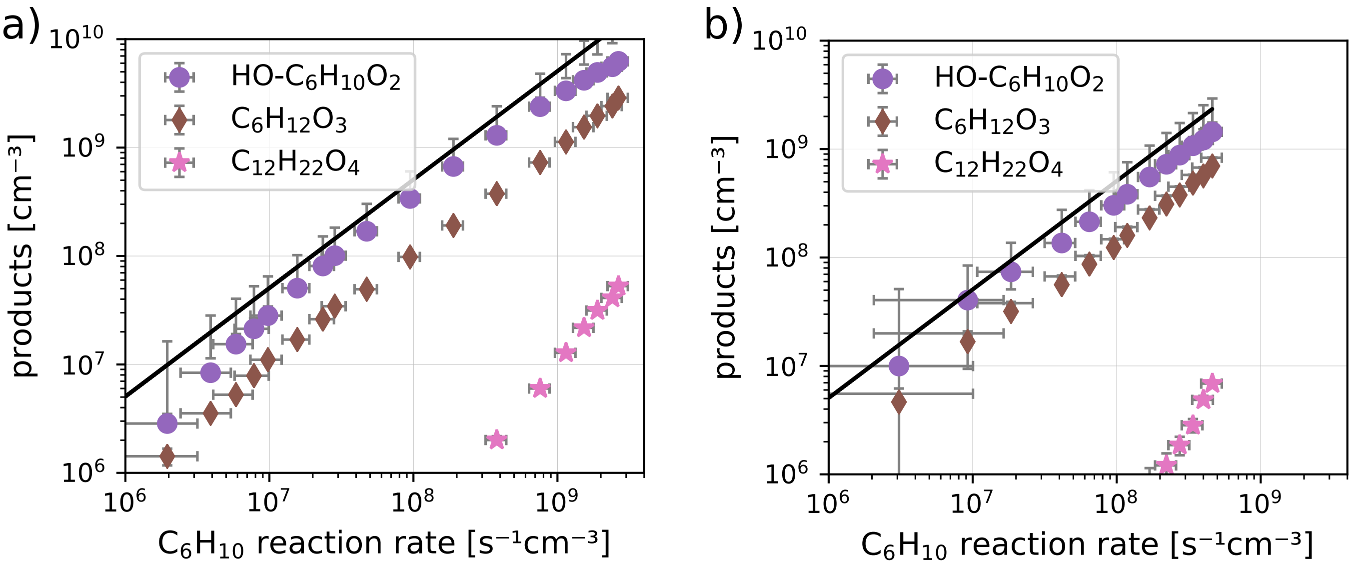

Figure S10 primary and secondary products of OH + C_6H_{10} during **(a)** *C_6H_{10}@TROPOS* experiment ([O_3] = $3.9 \cdot 10^{12}$ cm^{-3} constant, cyclohexene varied between $1.5 \cdot 10^{10}$ cm^{-3} < [C_6H_{10}] < $1.2 \cdot 10^{13}$ cm^{-3}) and **(b)** *C_6H_{10} (b)* experiment ([C_6H_{10}] = $3.8 \cdot 10^{12}$ cm^{-3} constant, ozone varied between $1.5 \cdot 10^{10}$ cm^{-3} < [O_3] < $1.4 \cdot 10^{12}$ cm^{-3}) The black line shows theoretically produced OH, considering cyclohexene ozonolysis as the dominant OH formation pathway. Shown are the peroxy radical, the main product of Cyclohexene + OH, making up 80% of all summed peroxy radicals (increasing linearly except for high production rates, when secondary reactions by self- and cross-reactions with other peroxy radicals become non-negligible, nicely visible in subfigure (a)), its presumable hydroperoxide (increasing linearly), and its accretion product from self-reaction (increasing quadratically as expected.)

Table S3 summarized data for calculating photolysis rates in the UVP ozone generator

wavelength [nm]		185	254
light intensity [mWcm^{-2}]		20	4
photon flux [cm^{-2}s^{-1}]		$7.5 \cdot 10^{14}$	$5.1 \cdot 10^{15}$
absorption cross sections [cm^2]	O_3	—	$1.13 \cdot 10^{-17}$
	O_2	$1.2 \cdot 10^{-20}$	—
	H_2O	$7.22 \cdot 10^{-20}$	—
photolysis rates AtChem [s^{-1}]			
$O_3 \rightarrow O(^1D) + O_2$		—	$5.76 \cdot 10^{-2}$
$O_2 \rightarrow O + O$		$8.94 \cdot 10^{-6}$	—
$H_2O \rightarrow H + OH$		$5.4 \cdot 10^{-5}$	—

The decrease of HO_2 is now less pronounced because the HO_2 concentration is lower. Finally, in stage 4, the VOC is added through the four impinging jets.

Running the simulation with differently long illuminated times in the ozone generator, we find that when producing a high ozone concentration in the reactor of $[O_3] = 2 \cdot 10^{12}$ cm^{-3}, the HO_2 concentration (under high water vapor assumption), would be $[HO_2] \approx 9 \cdot 10^{8}$ cm^{-3}, while for low ozone generation ($[O_3] = 2 \cdot 10^{11}$ cm^{-3}), we would get $[HO_2] \approx 1.8 \cdot 10^{8}$ cm^{-3}, meaning that under these conditions a ten-fold increase in ozone changes HO_2 by a factor of 5.

We can say, that the ozone generator is a source of HO_2 in our setup, but since its HO_2 production depends on its ozone production, we can not explain the observed nearly constant signal ratios between presumable hydroperoxides and peroxy radicals so far. Furthermore, the water vapor concentration should be significantly smaller than our high water vapor assumption, because the molecular sieves and additional active charcoal filter will adsorb left-over water molecules from the already dried air. Therefore we expect, that the actual HO_2 concentration in the reactor is substantially lower and other yet unknown pathways producing the observed signals at masses of $(ROOH)NH_4^+$ might exist. Because our reactor gives us the opportunity to partly decouple HO_2 concentrations from ozone by varying the time in stage 2 and water vapor in the flow through the UV lamp, it holds great potential to study RO_2+HO_2 reactions in the future.

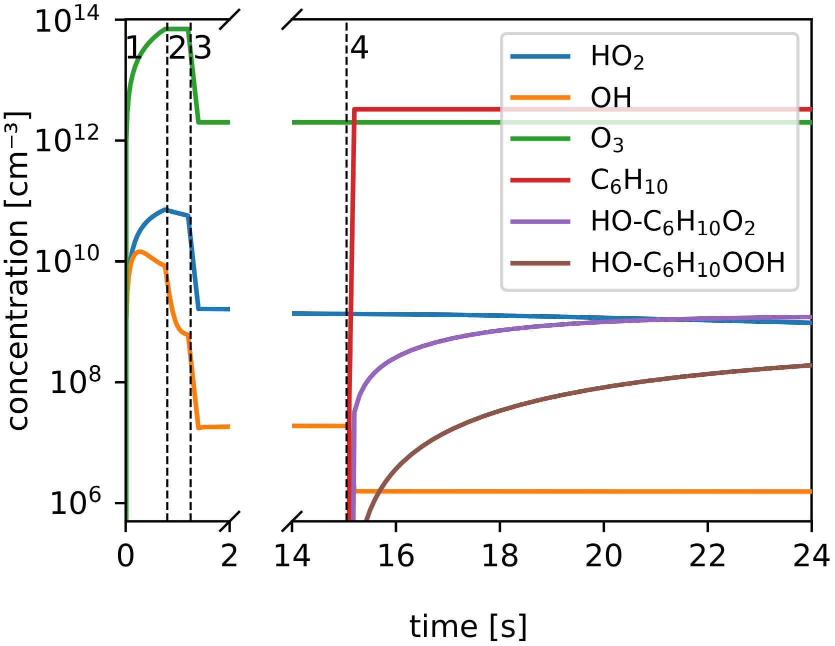

Figure S11 concentrations of selected compounds during a typical boxmodel simulation of the reactor with named stages. **1**: illuminated by the UV-lamp. **2**: before dilution, not illuminated. **3**: dilution by a factor 35, followed by ongoing reaction in the laminarization region. **4**: Reaction region: Cyclohexene is added. The water vapor concentration was set to "worst-case" $1 \cdot 10^{15}$ cm^{-3}.

S2.4 Kinetic analysis of accretion product formation

The kinetic analysis of accretion product formation is based on the assumption of linearly increasing peroxy radicals. Then,

$$
\begin{aligned}
\mathrm{ROOR}'(t) = \int_0^t \frac{\mathrm{ROOR}'}{d\tau} d\tau &= \int k_{dim}(\mathrm{RO_2}(\tau)\cdot \mathrm{R'O_2}(\tau))d\tau \\
&= k_{dim}(k_{\mathrm{O_3,VOC}}\cdot \alpha_{\mathrm{RO_2}}\alpha_{\mathrm{R'O_2}}\cdot [\mathrm{O_3}][\mathrm{VOC}])^2 \int \tau^2 d\tau \\
&= \frac{1}{3}k_{dim}(k_{\mathrm{O_3,VOC}}\cdot \alpha_{\mathrm{RO_2}}\alpha_{\mathrm{R'O_2}}\cdot [\mathrm{O_3}][\mathrm{VOC}])^2 t^3 \\
&= \frac{1}{3}k_{dim}\mathrm{RO_2}(t)\mathrm{R'O_2}(t)\cdot t
\end{aligned}
\tag{S37}
$$

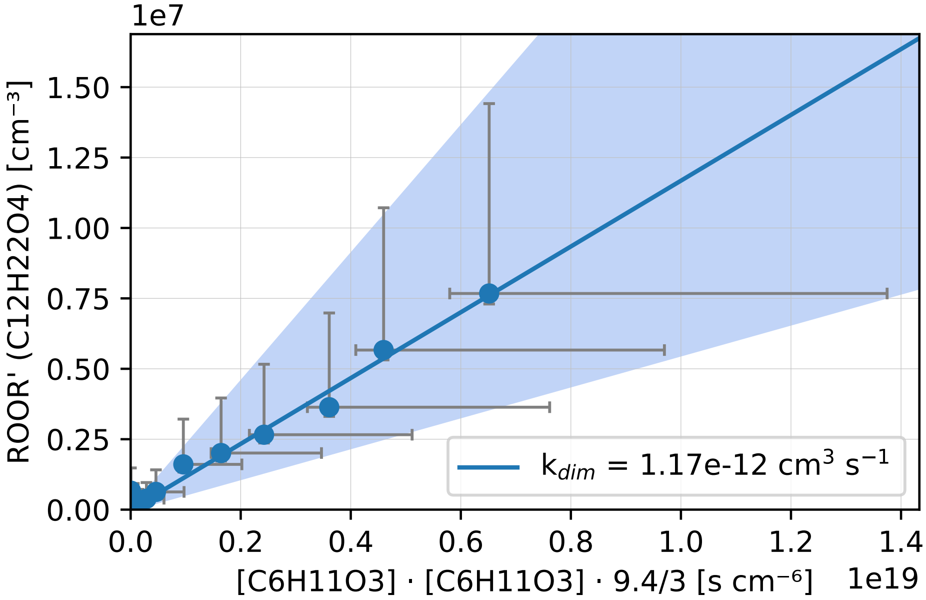

Figure S12 kinetic analysis of $C_6H_{11}O_3$ + $C_6H_{11}O_3$ accretion product formation in the INNpinJeR during experiment *C_6H_{10} (b)* (see table 1). The data are fitted with a function $f(x) = k_{dim} \cdot x$. The shaded area depicts the uncertainty of k_{dim} due to the possible systematic errors of the peroxy radicals and their accretion product (see sec. S1.4)

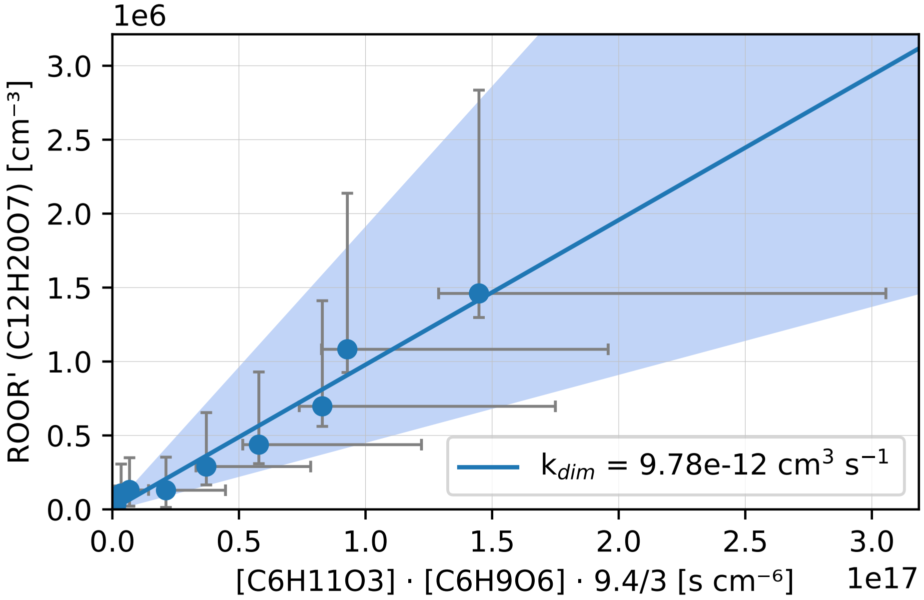

Figure S13 kinetic analysis of $C_6H_{11}O_3$ + $C_6H_9O_6$ accretion product formation in the INNpinJeR during experiment *C_6H_{10} (b)*. The data are fitted with a function $f(x) = k_{dim} \cdot x$. The shaded area depicts the uncertainty of k_{dim} due to the possible systematic errors of the peroxy radicals and their accretion product (see sec. S1.4)

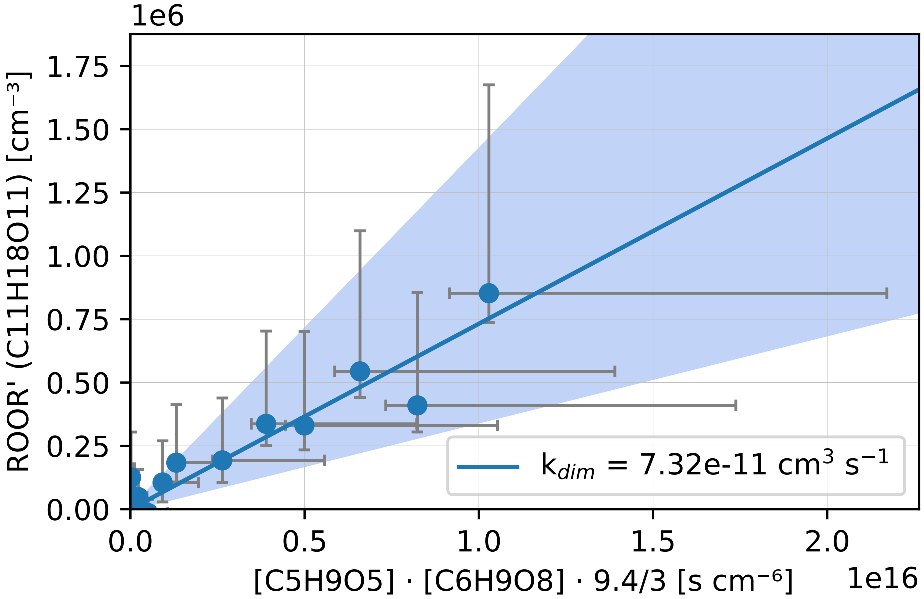

Figure S14 kinetic analysis of $C_5H_9O_5$ + $C_6H_9O_8$ accretion product formation in the INNpinJeR during experiment *C_6H_{10} (b)*. The data are fitted with a function $f(x) = k_{dim} \cdot x$. The shaded area depicts the uncertainty of k_{dim} due to the possible systematic errors of the peroxy radicals and their accretion product (see sec. S1.4)

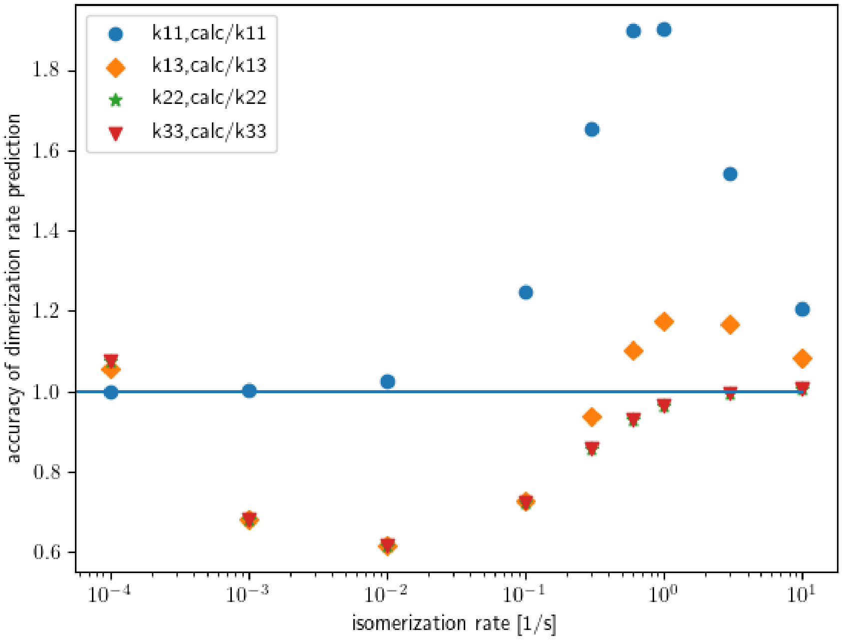

Figure S15 over- and underestimation of the accretion rate for different isomerization rates in the system of equ. S38.

S2.5 uncertainty in case of unknown peroxy radical isomerization rates

For cyclohexene, isomerization rate estimates for peroxy radicals from cyclohexene ozonolysis exist from earlier studies ([5]) and are fast enough to lead to a linear increase of the peroxy radicals with time[6].
In unknown cases, unaccounted isomerization rates can affect the increase of peroxy radicals in the flow reactor substantially and can affect e.g. calculated dimerization rates as performed above. To discuss, how big this effect can be, we will now look at a simple scenario in which bimolecular reactions are not significantly affecting peroxy radical concentrations. Isomerization acts as an additional loss or source of the different peroxy radicals. For the first peroxy radical in a line that undergoes isomerization, this will be a loss rate that is constant over time (and will therefore behave similar as the simulated constant loss by HO_2, when $k_{isom} \approx k_{HO_2+RO_2} \cdot HO_2$. The following peroxy radicals might on the other hand increase more than linearly over time as the isomerization can be an additional source term for them. Therefore, unknown isomerization rates can lead to further uncertainty of the accretion rates determined via equ. S37.
We modelled the peroxy radical and dimer behaviour with varying isomerization rates (in S38 b and c) in a simple 0D simulation with

$$A + B \xrightarrow{k} p1 \tag{S38a}$$

$$p1 \xleftrightarrow{k_{isom}} p2 \tag{S38b}$$

$$p2 \xleftrightarrow{k_{isom}} p3 \tag{S38c}$$

$$p1 + p1 \xrightarrow{k_{acc}} p11 \tag{S38d}$$

$$p1 + p3 \xrightarrow{k_{acc}} p13 \quad \text{etc. ...} \tag{S38e}$$

and found that it can lead to both over- and underestimation of the dimerization rates up to nearly a factor 2 as can be seen from fig. S15 if neglected. In the cyclohexene system, the isomerization rates are fast enough so that the peroxy radicals increase linearly with time as observed in the TROPOS reactor[6]. Therefore, the uncertainty due to RO_2 isomerization for the accretion product should be small for all accretion rates shown here. In unknown cases, it makes sense to determine the isomerization rates by e.g. NO- or HO_2-ramps to reduce the error of accretion rates.

References

[1] A. Hansel, W. Scholz, B. Mentler, L. Fischer and T. Berndt, *Atmos. Environ.*, 2018, **186**, 248–255.

[2] A. Zaytsev, M. Breitenlechner, A. R. Koss, C. Y. Lim, J. C. Rowe, J. H. Kroll and F. N. Keutsch, *Atmos. Meas. Tech.*, 2019, **12**, 1861–1870.

[3] J. Riegel, W. Mayer and Y. van Havre, *FreeCAD, version 0.18.4*, 2001-, `http://www.freecadweb.org`.

[4] J. Schöberl, *Comput. Visualization Sci.*, 1997, **52**, 41–52.

[5] M. P. Rissanen, T. Kurtén, M. Sipilä, J. A. Thornton, J. Kangasluoma, N. Sarnela, H. Junninen, S. Jørgensen, S. Schallhart, M. K. Kajos, R. Taipale, M. Springer, T. F. Mentel, T. Ruuskanen, T. Petäjä, D. R. Worsnop, H. G. Kjaergaard and M. Ehn, *J. Am. Chem. Soc.*, 2014, **136**, 15596–15606.

[6] T. Berndt, S. Richters, R. Kaethner, J. Voigtländer, F. Stratmann, M. Sipilä, M. Kulmala and H. Herrmann, *J. Phys. Chem. A*, 2015, **119**, 10336–10348.